nature communications

Article

https://doi.org/10.1038/s41467-025-66769-7

Mechanistic snapshots of lipid-linked sugar transfer

Received: 14 May 2025

Accepted: 14 November 2025

Published online: 06 December 2025

Check for updates

Ryan T. Morgan[1], Stefano Motta[2,13], Eva Gil-Iturbe[3,13], Biddut Bhattacharjee[4,13], Mohammad T. Anwar[5], Giovanni Di Muccio[6], Alice Romagnoli[6,7], Bedangshu Mishra[5], Khuram U. Ashraf[1], Injin Bang[1], Daniele Di Marino[6,7], Todd L. Lowary[5,8], Matthias Quick[1,3,9], Vasileios I. Petrou[10,11], Michael H. B. Stowell[4] ✉, Rie Nygaard[1,12] ✉ & Filippo Mancia[1] ✉

Enzymes undergo dynamic conformational changes during catalysis, yet conventional high-resolution structural methods typically capture only the most stable states. Here, we address this gap using rapid UV photolysis of a chemically caged substrate with cryogenic time-resolved electron microscopy (cryo-TREM). We elucidate the catalytic mechanism of GtrB, a membrane-bound glycosyltransferase that transfers glucose from UDP-glucose to the lipid carrier undecaprenyl phosphate. We visualized how GtrB, which has an active site ~15 Å from the membrane, transitions during the catalytic cycle to move each substrate in proximity for catalysis. From a single dataset, we resolved distinct conformational states: the initial substrate-bound state, a catalytically poised intermediate, and the product-bound state. Through molecular dynamics simulations and biochemical analyses, we identify coordinated movements within the active site that drive catalysis. These findings provide a molecular framework for understanding how glycosyltransferases function and highlight a broadly applicable strategy for capturing dynamic enzymatic states in native-like environments.

Enzymes are highly specialized machines that adopt distinct conformational states[1–4] during the various stages of their catalytic cycle. This is a prerequisite to ensure substrate specificity, efficient product release, and an energetically permissible chemical reaction, with molecular-level precision. Successful approaches for high-resolution structure determination, such as X-ray crystallography and single-particle cryo-electron microscopy (cryo-EM), are often limited by their intrinsic capability to capture only the lowest-energy conformations. Thus, the diverse ensemble of physiological enzymatic states is rarely accounted for in molecular-level structural analysis[5–7]. While recent

[1]Department of Physiology and Cellular Biophysics, Columbia University Irving Medical Center, New York, NY, USA. [2]Department of Earth and Environmental Sciences, University of Milano-Bicocca, Milan, Italy. [3]Department of Psychiatry, Columbia University Irving Medical Center, New York, NY, USA. [4]Molecular, Cellular & Developmental Biology, CU Boulder, Boulder, CO, USA. [5]Institute of Biological Chemistry, Academia Sinica, Nangang, Taipei, Taiwan. [6]New York-Marche Structural Biology Center (NY-MaSBiC), Department of Life and Environmental Sciences, Polytechnic University of Marche, Via Brecce Bianche, Ancona, Italy. [7]Neuronal Death and Neuroprotection Unit, Department of Neuroscience, Mario Negri Institute for Pharmacological Research-IRCCS, Milan, Italy. [8]Institute of Biochemical Sciences, National Taiwan University, Taipei, Taiwan. [9]Area Neuroscience - Molecular Therapeutics, New York State Psychiatric Institute, New York, NY, USA. [10]Department of Microbiology, Biochemistry and Molecular Genetics, New Jersey Medical School, Rutgers Biomedical and Health Sciences, Newark, NJ, USA. [11]Center for Immunity and Inflammation, New Jersey Medical School, Rutgers Biomedical and Health Sciences, Newark, NJ, USA. [12]Department of Radiation Oncology, Weill Cornell Medicine, New York, NY, USA. [13]These authors contributed equally: Stefano Motta, Eva Gil-Iturbe, Biddut Bhattacharjee. ✉e-mail: stowellm@colorado.edu; rin7007@med.cornell.edu; fm123@cumc.columbia.edu

studies using microfluidic spray-plunging[8,9] or sequential time-point freezing[10–12] have shown promise, few if any, molecular-level snapshots of enzymes across their complete catalytic cycle exist. To address this limitation, we focused on the catalysis of lipid glycosylation, one of the most common reactions found on cellular membranes across all domains of life carried out by glycosyltransferases (GTs).

The first step in all extracellular glycan synthesis typically requires the generation of membrane-embedded sugar conjugates containing polyisoprenyl phosphate (PP) - or pyrophosphate - lipid carriers[13,14]. In Gram-negative bacteria, GTs use a universal PP carrier, undecaprenyl phosphate (UndP), a 55-carbon isoprenoid, to carry sugars across the membrane for synthesis and modification of structures such as lipopolysaccharide and peptidoglycan[15,16]. In eukaryotes, a similar PP, dolichol phosphate (DolP), carries an oligosaccharide as a donor for N-linked protein glycosylation[13,17]. PP sugar carriers are synthesized by a class of membrane-attached GTs, referred to as acceptor polyisoprenyl phosphate GTs (PP-GTs)[18]. These enzymes often function through a metal-dependent inverting displacement reaction, facilitating the transfer of a monosaccharide from a sugar nucleotide onto a PP[19]. Despite the functional and ubiquitous nature of this process in cellular function, we lack a molecular-level understanding of how PP-GTs function. A handful of currently available structures show that the reaction between the phosphate headgroup of the polyprenyl and the nucleotide-activated sugar occurs within a soluble glycosyltransferase domain of the GT-A or GT-B fold superfamily, located ~15–20 Å from the membrane leaflet[18,20–23]. This considerable molecular distance raises an intriguing biophysical question as to how the membrane-embedded lipidic substrate and the distant active site come in contact for catalysis.

Here, we focused on GtrB from *Synechocystis* sp. PCC6803, which was the first reported acceptor PP-GT structure[20], and shares structural homology to GTs across all kingdoms of life[21,22,24]. GtrB catalyzes the transfer of glucose (Glc) from UDP-Glc onto UndP to form UndP-Glc (Fig. 1a). This product is used as a donor for serotype conversion of the O-antigen in Gram-negative strains, a mechanism of immune evasion in bacteria[25,26] (Supplementary Fig. 1a). To capture an ensemble of catalytic states, we synthesized a caged photolabile UDP-Glc derivative, allowing substrate binding without initiating catalysis. Following rapid

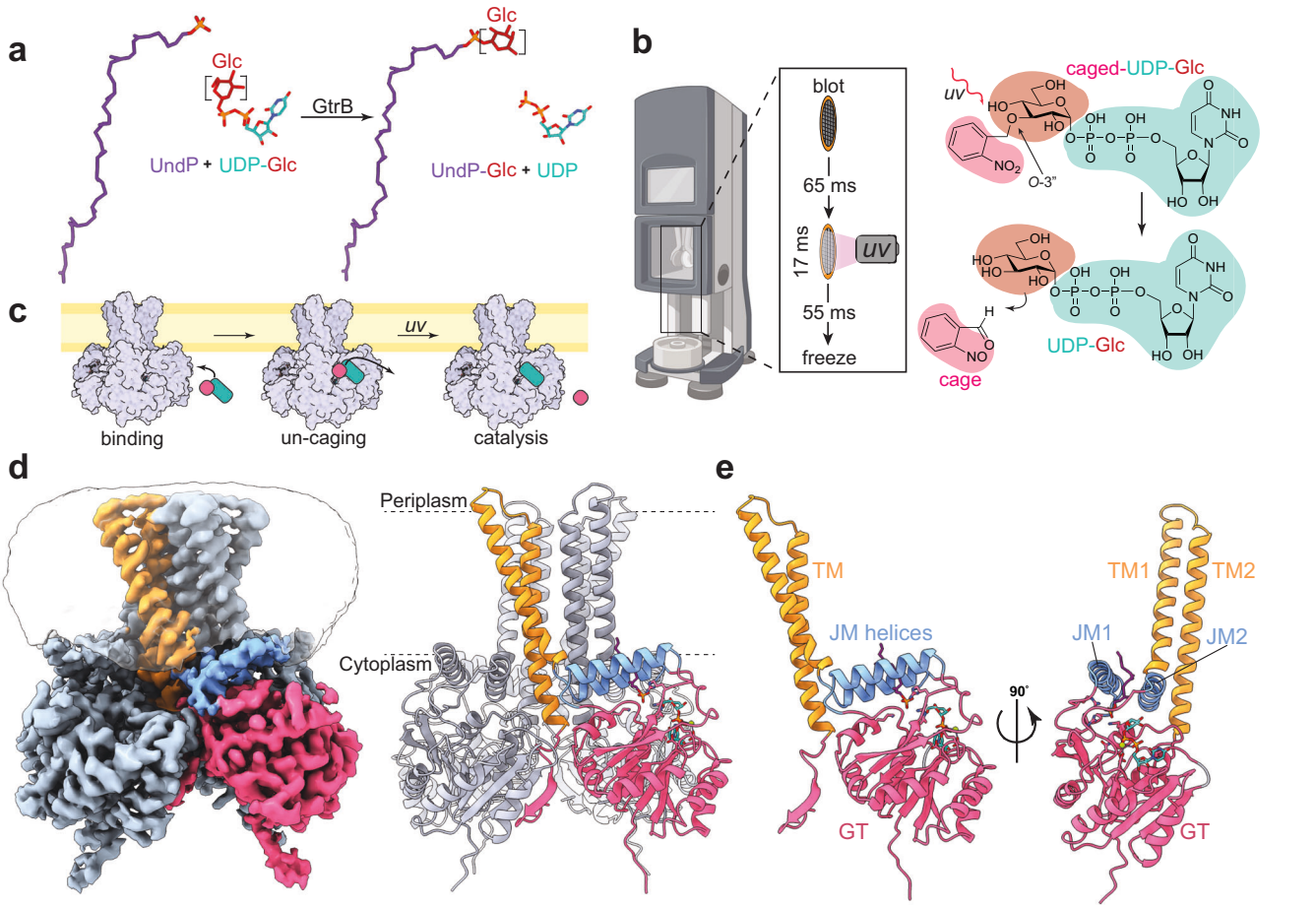

Fig. 1 | Time-resolved cryo-EM of the glycosyltransferase GtrB. a Reaction catalyzed by GtrB. The Glc moiety (maroon) on UDP-Glc (teal) is transferred onto the UndP (purple) headgroup by GtrB, forming UndP-Glc. See also Supplementary Fig. 1a for the cellular role of GtrB. **b** Cartoon representation of 'Flash-and-freeze' system for cryo-TREM showing the travel of the cryo-EM grid before being vitrified on the left. On the right, the uncaging of 3"-*O*-(2'-nitrobenzyl)-UDP-Glc by UV irradiation forming free UDP-Glc (cyan and maroon) and a cage byproduct (pink). Portions of this panel were created in BioRender (Morgan, R. (2025) https://BioRender.com/z7vy4nk) (**c**) Cartoon of theoretical un-caging (pink) of UDP-Glc (teal) when bound to membrane-embedded GtrB after UV irradiation resulting in catalysis. Portions of this panel were created in BioRender (Morgan, R. (2025) https://BioRender.com/z7vy4nk) (**d**) Cryo-EM density map of the substrate-bound state GtrB bound to UndP and UDP-Glc. The density corresponding to a single protomer is colored, while the remaining three protomers are colored grey. Coloring is as follows: TM domain (orange), JM helices (light blue), and soluble GT domain (pink). On the right, the ribbon model of the substrate-bound state is shown with approximate membrane boundaries represented as dotted lines (**e**) Ribbon model of a GtrB protomer with TM1 and TM2 colored orange, JM1 and JM2 colored light blue, and the GT domain colored pink. The right-hand side shows a 90° rotation.

UV photolysis on the grid, the cage is released and immediately thereafter vitrified for cryo-EM using a 'flash-and-freeze' plunge-freeze system, trapping nanodisc-incorporated enzyme with PP in various states along the reaction trajectory. Our cryogenic time-resolved electron microscopy (cryo-TREM) approach resulted in structures with both substrates, of an intermediate state primed for catalysis, and of the product-bound state. Combining structural information, molecular dynamics simulations, and biochemical assays allowed us to decipher the entire catalytic cycle of GtrB in molecular detail.

Results

Structure determination of apo-GtrB

To establish the model system before cryo-TREM, GtrB from *Synechocystis* sp. PCC6803 was overexpressed and purified in detergent, as previously described[20], and reconstituted into lipid-filled nanodiscs (Supplementary Fig. 1b–d) for structure determination by cryo-EM. After collecting ~3700 micrographs on a Technai Polara electron microscope with a K3 direct electron detector, particles were sorted by 2D-classification, volumes separated by heterogeneous refinement, and refined to yield a 2.79 Å resolution density map. Into this map, we successfully modeled the structure of apo-GtrB (Supplementary Fig. 1e–h), which closely resembles the previously published UDP-bound GtrB crystal structure[20] (Supplementary Fig. 1i). GtrB is a homotetramer in which each protomer consists of a soluble domain, which bears the classical GT-A superfamily fold with two β/α/β Rossmann-like nucleotide-binding domains tightly associated to resemble a single domain (Supplementary Fig. 2a)[19,27]. This extends into the membrane with two juxtamembrane (JM) helices, a common structural element found in related GTs[21], and two transmembrane (TM) helices that form an eight-helix TM bundle (two TM helices per protomer of the tetramer). Both β5-JM1 and β7-JM2 loops lack interpretable density, similar to what was previously observed. The GT-A domain of apo-GtrB is structurally homologous to that of the crystal structure with a root-mean-square-deviation (RMSD) of 1.9 Å among backbone atoms (Supplementary Fig. 2b). The primary difference is within the TM helix domain, where improved density in the periplasmic TM1-TM2 loop of the apo map revises the original assignment of TM helix 2 in the tetrameric assembly (Supplementary Fig. 2c, d). This results in an arrangement where TM helix 2 and the C-terminal domain interact with the adjacent protomer in the tetrameric assembly. Accounting for this difference and comparing over an entire protomer shows an RMSD of 2.3 Å among the backbone between the apo-GtrB and the crystal structure.

While GtrB is a tetramer, we predominantly observe a non-physiological tail-to-tail octamer among the particles collected (Supplementary Fig. 1e). This was previously seen in the crystallographic analysis of GtrB and assumed to be due to crystal-packing[20]. We find it originates from a stacking interaction mediated by Q58 and R61 between tetramerized particles. Attempts to purify a Q58S-R61T double-mutant tetramer were made, but the majority of the protein aggregated, hampering nanodisc incorporation and limiting the overall yield (Supplementary Fig. 2e, f).

'Flash-and-freeze' system for cryo-TREM of substrate-bound GtrB

We developed a cryo-TREM approach using a caged substrate in conjunction with a modified UV-LED mounted plunge-freeze system, as previously described[28] (Fig. 1b, c). This approach relies on the controlled release just before vitrification of a 'cage' from a catalytically inert compound, thereby liberating an active substrate. To this end, we synthesized a caged-derivative of UDP-Glc[29], 3-*O*-(2'-nitrobenzyl)-UDP-Glc (Supplementary Fig. 3a), which exploits the photolabile properties of 2-nitrobenzyl ethers to protect the Glc moiety from nucleophilic attack until UV exposure removes the cage (Fig. 1b). By applying short UV irradiation, it ensures minimal heating to the sample[28] while allowing for rapid uncaging of UDP-Glc. To test optimal substrate release at saturating concentrations, a standard curve was determined using the photolysis system combined with HPLC quantification with a photostable internal standard (Supplementary Fig. 3b-d).

Detergent-solubilized GtrB was reconstituted into nanodiscs with 10% w/w UndP to lipid and mixed with caged-UDP-Glc. After application of the sample and blotting, the grids traveled through a focused UV beam for 17 ms, reaching the liquid ethane bath after 55 ms (Fig. 1b), before being vitrified within 1 ms[30,31] for subsequent cryo-EM analysis. After collecting ~9200 micrographs on a Titan Krios electron microscope with a K3 direct electron detector, particles were sorted by 2D-classification and subsequent 3D-heterogeneous refinement to yield a 2.54 Å density map of GtrB in C4 symmetry (Fig. 1d, e; Supplementary Fig. 4). Here, we find clear density for both UndP, held within the JM helices, and UDP-Glc bound in the active site. We refer to the resulting structure as the substrate-bound state (Fig. 2a). Through subsequent rounds of 3D-variability analysis (3DVA) and 3D-classification, as implemented in cryoSPARC v4.6.2[32,33], we observed heterogeneity within the TM domain, JM helices, and the substrate binding pocket (Supplementary Movie 1). Particle sets were further separated by conventional 3D-classification to obtain two distinct states of GtrB along its catalytic cycle. First, in a 2.85 Å structure that we refer to as the pre-catalysis state, UndP is positioned near UDP-Glc, deep inside the active site (Fig. 2b). Second, within the same map, a different protomer contained density for the reaction products, UDP and UndP-Glc, which we consider the product-bound state (Fig. 2c).

Although octameric particles were most prevalent, as in the apo dataset, a small fraction (~ 4.5%) of GtrB tetramer particles were also observed in this dataset. These were classified, leading to a 3.19 Å cryo-EM map (Supplementary Fig. 4a). This map exhibits a poorer density in the periplasmic TM loop and C-terminal domain but is largely identical (correlation value of 0.86) to the octamer, substrate-bound map (Supplementary Fig. 4e). During 3D-classification, we chose to use D1 symmetry-expanded particles instead of D4, which reduced the dataset size and produced maps with greater clarity, while still accounting for tetramer-wide variations.

UndP and UDP-Glc substrate-bound GtrB

In the substrate-bound state of GtrB, we found unambiguous density for UndP in between JM helices 1 and 2 (Supplementary Fig. 5a). The UndP headgroup is bound in a hydrophilic pocket below JM1 containing R122, R125, K132, and K180 (Fig. 2a). R122 is universally conserved among GT-A acceptor PP-GTs[18], while R125 appears partially conserved[20,23], and it was previously shown that their mutation abolished activity[20]. The tail of UndP extends upwards into the membrane, though only five isoprenyl units are resolved in the map, making it difficult to interpret if and how the tail associates with the TM domain. In the GT-A domain, there is well-defined density for UDP complexed with a Mg^{2+}-ion coordinated partially by the conserved Asp-X-Asp (DxD, in this case D96) motif (Fig. 2a). Extending from UDP, we model as the Glc moiety, albeit with weaker density (Supplementary Fig. 5a) than surrounding regions likely due to a lack of strong coordination of the sugar residue, resulting in considerable rotational freedom within the active site. When comparing the substrate-bound state to the apo structure, both JM1 and JM2 are shifted laterally (Supplementary Fig. 5b). While the density in this region is of poorer quality in the apo map, the JM helices become ordered in the substrate-bound state, forming a hydrophobic tunnel for the polyprenyl chain. We also observed shifts in the TM domains (Supplementary Fig. 5c), suggesting that the acyl chain of bound UndP may slightly alter the arrangement of the TM bundle.

The UndP headgroup is positioned ~9.5 Å from the electrophilic C1 of Glc, and a similar distance from D157, the previously hypothesized catalytic residue[20] (Supplementary Fig. 6a). Therefore, significant movement from either or both substrates would be required to allow

https://doi.org/10.1038/s41467-025-66769-7

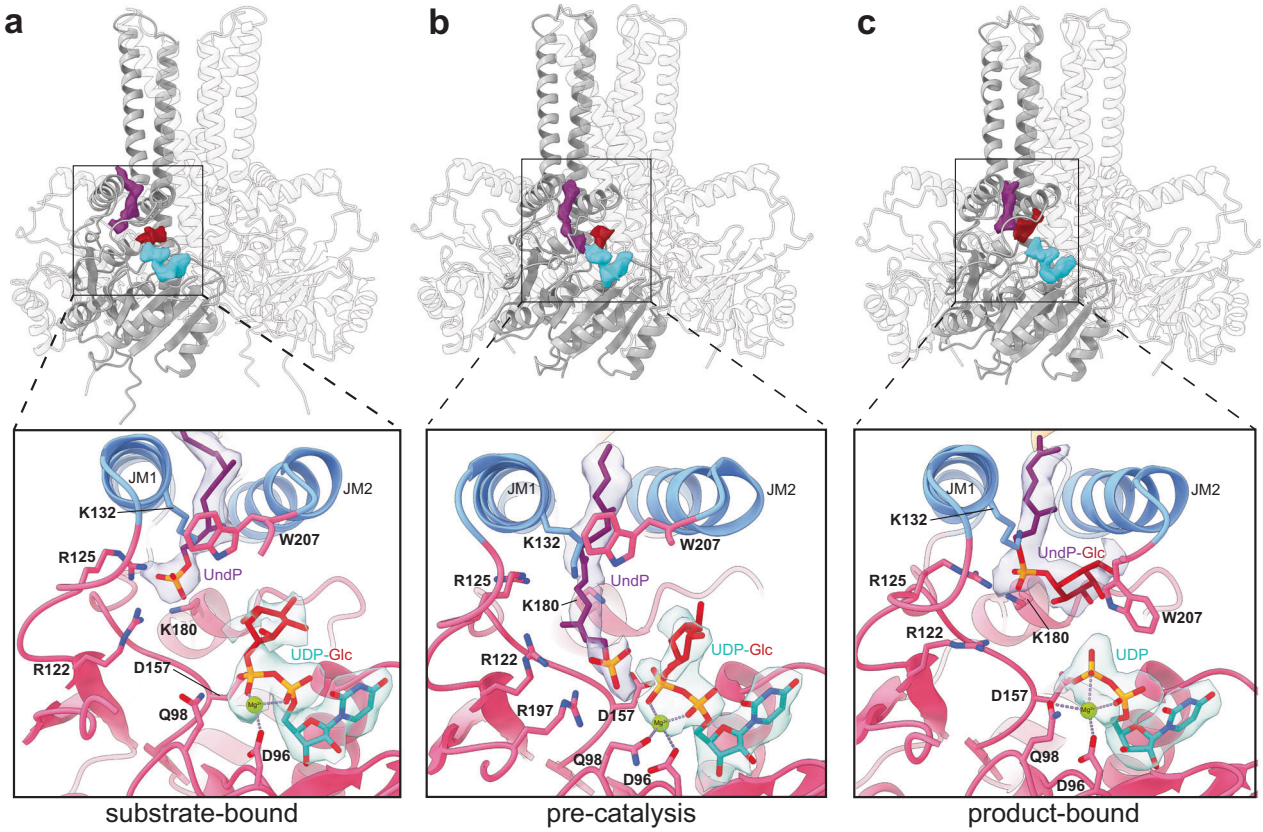

Fig. 2 | Comparison of the three states of GtrB catalysis. a On top, a ribbon model of the substrate-bound state colored by a single protomer in grey and the remaining structure as translucent white. The bound UndP density is shown in purple, bound UDP-Glc is colored by UDP (teal) and Glc (maroon). See also Supplementary Fig. 5a for density in respective regions. On the bottom, a zoom-in of the corresponding protomers colored as in Fig. 1. Translucent density corresponding to UndP (purple) and UDP-Glc (teal) are shown with relevant residues labeled. The same is shown for the pre-catalysis state (**b**) and product-bound state (**c**).

the reaction to occur. While our use of cryo-TREM in this context makes it difficult to understand the precise temporal placement of this state in the reaction coordinate, it remains the dominant structure encompassing over 80% of the particle dataset, suggesting this is a stable state adopted by GtrB following initial binding of substrates.

Pre-catalytic state of GtrB

Through 3D-classification, we determined a pre-catalysis state where the density for UndP extends deeper into the soluble domain, shifting from the pocket of R125 and R122 onto R197 and just underneath C1 of the Glc (Fig. 2b, Supplementary Movie 2). The phosphate headgroup is located 4.6 Å from the Glc C1, a distance that is permissible for nucleophilic attack. However, it is farther from D157 (~ 10.3 Å) compared to the substrate-bound state (Supplementary Fig. 6b), suggesting this state could exist after the initial deprotonation of UndP. Near the UDP-Glc, D96 remains coordinated to Mg^{2+} but is joined by Q98, which flips towards the ion while the Glc moiety is slightly rotated to accommodate the UndP tail (Fig. 2b). The UndP headgroup is shifted downwards ~ 9 Å from the substrate-bound state, but the UDP moiety has not moved, suggesting that UndP translocation is a key factor in catalysis. Interestingly, the TM bundle in the pre-catalysis state closely matches the TM domain in the apo structure (Supplementary Fig. 5d), whereas the differences in JM1 and JM2 position are comparable to what was observed in the substrate-bound state (Supplementary Fig. 5e). The density for Glc is also well-defined suggesting that at least within this state, Glc may have less freedom to remain flexible in the active site compared to our substrate-bound state. However, the density in the β7-JM2 loop is poor and wasn't sufficient to fully model.

Product-bound state of GtrB

In the same map as the pre-catalysis state, we observe density in a different protomer that we interpret as UndP-Glc and UDP, the products of the reaction. Interestingly, the product-bound state appears to best match the substrate-bound state in relation to both UndP, located towards R125 and R122 (Fig. 2c), and UDP position, but several key differences do arise (Fig. 2, Supplementary Fig. 6c). In particular, the Glc moiety of UndP is underneath JM2 and appears to interact with W207 along the β7-JM2 loop (Fig. 2c). The density in the β7-JM2 loop after W207 is weak and therefore wasn't modeled, consistent with our pre-catalytic state, limiting our understanding of how this loop contributes to product coordination. However, W207 in both the pre-catalysis and substrate-bound states is flipped inward in front of the UndP, but here, it faces away from the Glc, opening a potential path for the product to exit toward the membrane (Fig. 2, Supplementary Movie 3).

Conformational and molecular dynamics of the pre-catalytic state

In 3DVA intermediate volumes within the cryo-TREM dataset, the β6-JM1 loop oscillates up and down in conjunction with JM1 (Fig. 3a, Supplementary Movie 1), while JM2 remains largely static. When comparing the modeled pre-catalysis and substrate-bound states, the β6-JM1 loop is ~4.4 Å lower along with the end of JM1 (Fig. 3b). Interestingly, the lowered position of the β6-JM1 loop is also observed in the product-bound state (Supplementary Fig. 6e). This coincides with an ~8.9 Å shift of UndP from the substrate-bound state (Fig. 3b), suggesting that lowering of the β6-JM1 loop toward the cytosol correlates with UndP translocation to the C1 of Glc (Supplementary Movie 2).

https://doi.org/10.1038/s41467-025-66769-7

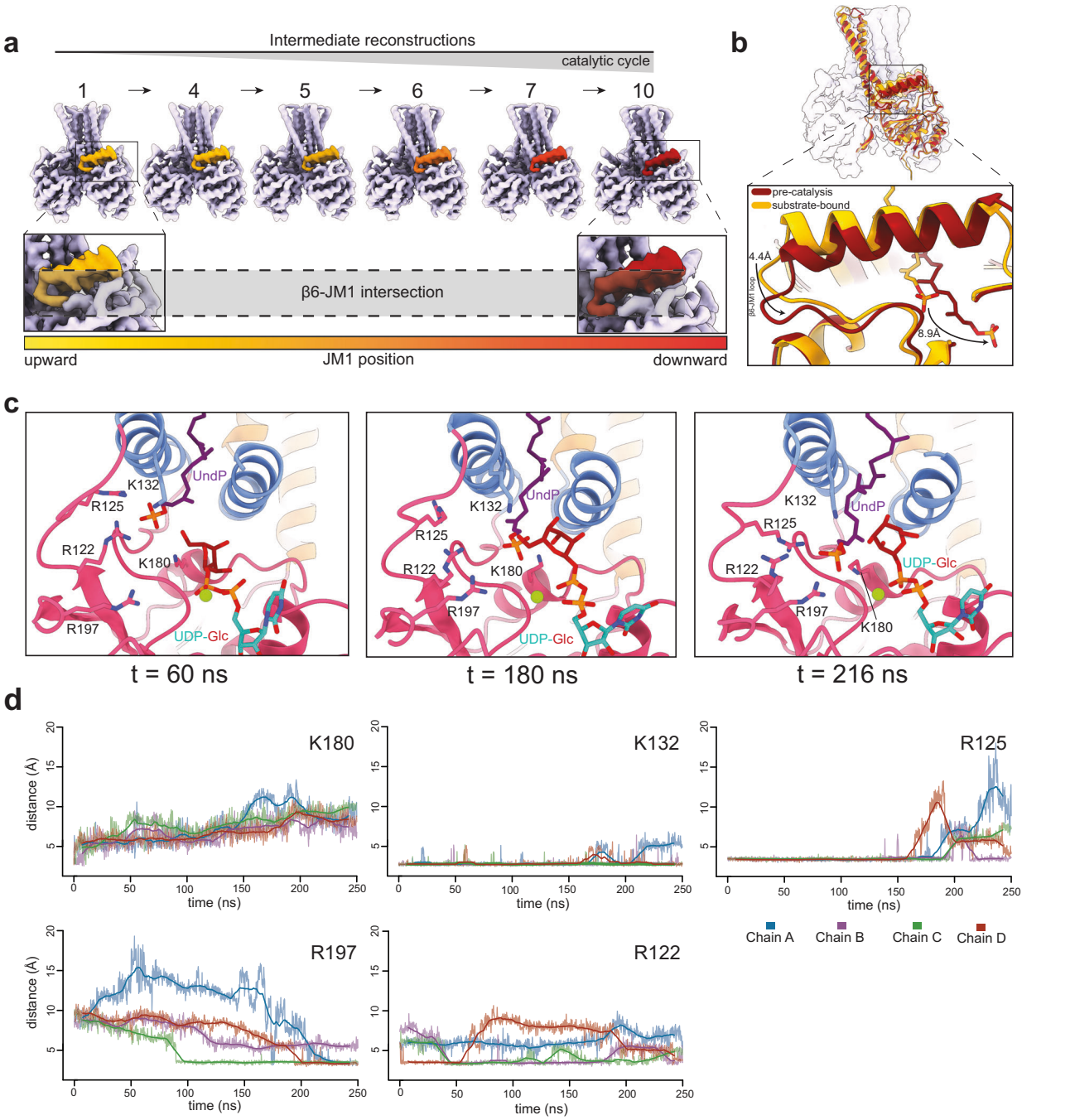

Fig. 3 | Dynamics in the pre-catalysis state. a 3DVA intermediate volumes of dynamics within the dataset. Using the 3DVA function of cryoSPARC, particles were divided to obtain 10 reconstructions across the major principal component of motion. Only frames that exhibit significant differences from the previous one are shown (frames 2–3 and 8–9 are excluded). Reconstructions shown include the sharpened maps in solid color (light purple and JM1 colored relative (gradient yellow to red) to its position from an upward state (frame 1) to a downward state (frame 10). A zoom-in of Frame 1 vs. Frame 10 illustrates a downward displacement of JM1 within the intersection of the β6 loop and the end of JM1 represented by a dotted line. **b** The density map of frame 1 is overlaid to the density map of frame 10, with volumes rendered translucently (light purple) overlaid ribbon models of the substrate-bound state protomer (yellow) and the pre-catalysis state protomer (maroon). On the bottom, a zoom-in of the JM1 region showing distances between each state. The β6 loop lowers by ~4.4 Å (measured from T147 on contrasting models) and a displacement of the UndP by 8.9 Å (measured from the phosphate group on contrasting models).**c** Time-series snapshots from SMD simulations initiated from the substrate-bound state. Ribbon representations are colored as in Fig. 1. From t = 60 ns to t = 216 ns, UndP descends into the active site towards R197, breaking previous interactions with R125, K180, and K132. **d** Distance plots from SMD simulations depicting the relative positioning of select residues to the UndP headgroup. Each chain of the substrate-bound state is colored in blue, purple, green, and red. As UndP descends into the active site, R125 moves away, K132 and K180 follows its descent, and R197 approaches to establish coordination by t = 216 ns.

Although JM2 remains stationary, the directly connected TM2 also oscillates vertically in 3DVA intermediates (Supplementary Movie 1).

Unbiased molecular dynamics (MD) simulations were performed on the GtrB tetramer, with analyses conducted separately for each of its four chains. To ensure the robustness of our findings, the stability of each state was confirmed using two different water models (TIP3P and OPC), which yielded highly congruent results (Supplementary Fig. 7 and 8). In simulations of both the substrate-bound and pre-catalysis state models, root mean square fluctuation (RMSF) analysis indicates greater flexibility in JM1 and JM2 in the pre-catalysis state compared to the substrate-bound state (Supplementary Fig. 9a, b). In the substrate-bound state simulation, K180 and K132 remain proximal to the phosphate of UndP but do not maintain stable coordination over time (Supplementary Fig. 9c, d). As expected, UndP remains stable in this conformation and does not spontaneously transition to the pre-catalysis state within the simulation time (Supplementary Fig. 9e), indicating the presence of a local free energy minimum due to the coordination of the phosphate headgroup in the positively charged pocket. Conversely, in unbiased MD simulations of the pre-catalysis state, R122 and R197 emerge as the dominant coordinating residues, while R125, K132, and K180 are positioned farther from the phosphate headgroup than in the substrate-bound state (Supplementary Fig. 10a–e). UndP remains partially stable in this intermediate conformation, with only one out of four chains reverting to a substrate-bound-like arrangement, persisting near R122 and R197 (Supplementary Fig. 10f).

Steered molecular dynamics (SMD) simulations were conducted to investigate the translocation mechanism of UndP towards the Mg^{2+} starting from the substrate-bound state. These simulations reveal a gradual descent of UndP within the active site (Fig. 3c, Supplementary Movie 4), with K180, K132, and R125 initially coordinating the phosphate headgroup and facilitating translocation. As UndP progresses, R122 and R197 overtake as the primary coordinators (Fig. 3d). Essentially, K132 and K180 remain closely associated with UndP as it moves downward (t = 60–216 ns), while R125 initially engages (t = 60 ns) but subsequently transfers coordination to R197 and R122 (t = 216 ns, Fig. 3c-d). The center-of-mass (COM) displacement of JM1 in these simulations follows a directed motion along the z-axis, reaching deviations of approximately 6 Å (Supplementary Fig. 9f), similar to what was observed in the pre-catalysis and product-bound states. The work profiles for all SMD replicates were analyzed to estimate the free energy barrier (Supplementary Fig. 11a). The analysis of the lowest-work trajectory, which is the dominant contributor to the Jarzynski average, suggests a maximum barrier lower than 12 kcal/mol (~ 20 kBT), indicating a physically accessible and rapid transition (Supplementary Fig. 9g).

UndP-Glc exits laterally toward the membrane through a molecular gate

A major structural difference in the product-bound state lies in W207, which appears swung out on the β7-JM2 loop, opening a path for the lipid carrier to exit the active site into the membrane (Fig. 4a, Supplementary Movie 3). In similar enzymes such as the archaeal DolP Mannose Synthase (DPMS), this loop has been proposed to act as a 'door', letting substrates and products enter or exit the active site[21].

In unbiased MD simulations of the product-bound state, we show the product (UndP-Glc) remains stable without an input of force (Supplementary Fig. 10h). To model the conformational dynamics following product formation, additional SMD simulations were performed using the product-bound state with the full-length β7-JM2 loop modeled using the substrate-bound state as a reference (Supplementary Movie 5). Here, the phosphate head of UndP-Glc was pulled away from the reaction site (specifically from the Cα of K180), towards the β7-JM2 loop. The work profiles for all SMD replicates of the product exit process were analyzed to characterize the transition (Supplementary Fig. 11b). The lowest-work trajectory, which best represents the Jarzynski-weighted ensemble, shows a near-spontaneous shift of UndP-Glc with an initial negative force barrier, followed by additional work needed as the β7 loop accommodates the UndP tail (Supplementary Fig. 10g). At the start of the simulation (t = 0 ns), W207 is in a conformation characteristic of the product-bound state (Fig. 4b), leaving an open pathway towards the membrane. As the simulation progresses, W207 gradually rotates, further widening the exit for UndP-Glc, which eventually translocates beneath the β7-JM2 loop (t = 200 ns; Fig. 4b). Superimposing the initial (t = 0 ns) and final (t = 200 ns) states highlights a lateral displacement of UndP-Glc towards the membrane, coupled with a coordinated rotation of W207 that facilitates its release (Fig. 4b). Throughout this transition, R125 and K180 initially coordinate the phosphate headgroup of UndP-Glc in a similar fashion to the substrate-bound state before the product exits (Fig. 4c).

Enzymatic Kinetics of GtrB

To understand the kinetics of GtrB independent of cryo-TREM, we performed functional studies of GtrB in a reconstituted setting by measuring equilibrium binding and sugar transfer kinetics.

Using a scintillation proximity assay[34], we tested binding of radiolabeled UDP-[^{14}C]-Glc to GtrB incorporated in nanodiscs. Our results demonstrate that GtrB binds UDP-Glc with an affinity of 114.4 μM, comparable to that of caged-UDP-Glc (Fig. 4d). Additionally, UDP-galactose (UDP-Gal), as well as Glc or UDP alone, also bind GtrB, albeit with slightly lower affinity. Notably, the addition of 50 μM UndP to the binding assay increased the binding affinity for UDP-[^{14}C]-Glc by 32%, suggesting cooperative interactions between the donor and acceptor substrates (Fig. 4d).

To characterize the kinetics of Glc transfer to membrane-embedded UndP, proteoliposomes containing GtrB and 200 μM UndP (Supplementary Fig. 12a) were subjected to UDP-[^{14}C]-Glc incorporation assays. Expectedly, GtrB-containing proteoliposomes show a progressive increase in [^{14}C]-Glc incorporation over time (Fig. 4e). In contrast, all tested mutants – targeting the catalytic site (D157), Mg^{2+} coordination site (Q98), and the W207 gate between the β7-JM2 loop – exhibited significantly lower incorporation levels that limited conclusive kinetic analyses.

Lastly, we determined GtrB-mediated [^{14}C]-Glc incorporation to membrane-bound UndP, measured for 10-second periods by varying the concentration of UDP-[^{14}C]-Glc from 1 nM to 2.5 μM, revealing a Michaelis–Menten constant (K_m) of 0.23 ± 0.03 μM and a V_{max} of 8.99 ± 0.38 mmol mg GtrB^{-1} min^{-1}, resulting in a catalytic turnover rate (k_{cat}) of 4.77 ± 0.33 s^{-1} (Supplementary Fig. 9b). Thus, the incorporation affinity of UDP-Glc during catalysis is estimated to be 500-fold higher than the binding affinity of UDP-[^{14}C]-Glc to GtrB alone.

Our kinetic assays on proteoliposomes likely favor tetramer formation, but in our previous study[20], we performed kinetic assays on crude, solubilized membranes. In both, we yield similar results, particularly that mutation of D157 abolishes catalytic activity despite this not being a conserved residue among membrane-bound GT-A enzymes. Thus, it could suggest that individual GtrB monomers act independently in catalysis, rather than in an allosteric model.

Proposed mechanism of GtrB catalysis

We propose a sequence of events that results in the catalysis of UndP-Glc by GtrB (Fig. 5a, b). First, membrane-embedded UndP binds GtrB through the JM helices. Based on our apo structure and previous findings[20], the N-termini of both JM1 and JM2 remain disordered until binding of UndP, which stabilizes the two helices. The UndP headgroup is then stabilized in a pocket lined by K132, K180, R125, and R122. UDP-Glc binds in a conserved pocket lined by Q98, and the DxD motif (D96 and D94). Following the initial binding event, the UndP headgroup interacts primarily with K180, K132, and R125 until it reaches

https://doi.org/10.1038/s41467-025-66769-7

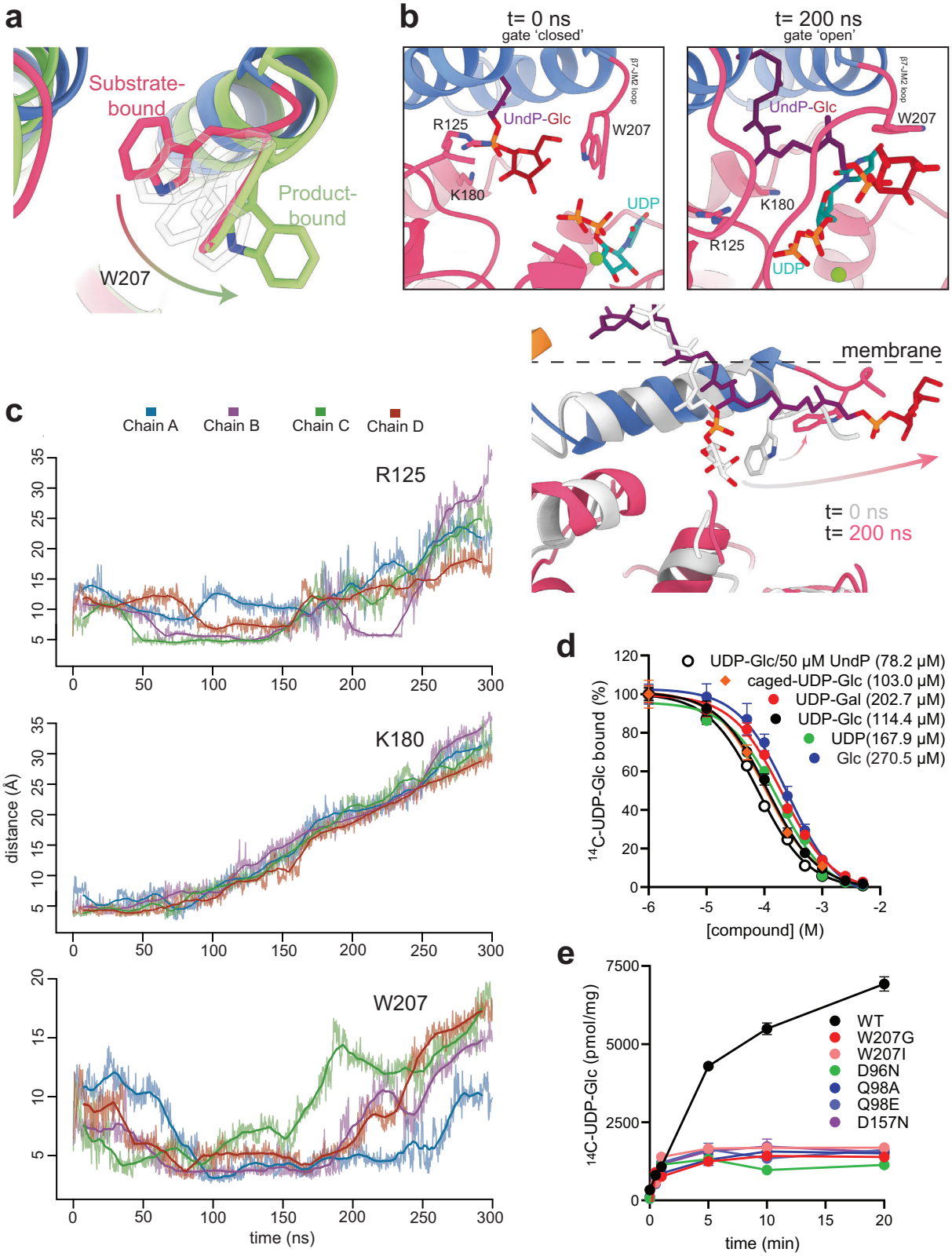

R197. This coincides with a downwards shift in JM1 and the β6-JM1 loop. In this position, UndP is in proximity to the Glc C1, primed for the enzymatic reaction. Product formation is associated with a return of UndP towards the original bound position, with an added Glc moiety. Exit is mediated by an interaction with W207 acting as a gate for the β7-JM2 loop which subsequently opens to allow exit of the product into the membrane.

The reaction catalyzed by GtrB is dependent on Mg^{2+}, similar to GTs that use nucleotide diphosphate sugars as substrates[19]. In inverting glycosyltransferases, nucleophilic attack by the acceptor hydroxy group leads to an inversion of stereochemistry at the anomeric center of the donor substrate. These enzymes typically use a catalytic base and a bound metal ion that stabilizes the leaving diphosphate nucleotide. One candidate for the catalytic base in GtrB, formerly

https://doi.org/10.1038/s41467-025-66769-7

Fig. 4 | Product exit pathway and dynamics in the product-bound state. **a** Flipping of W207 between the substrate-bound state (pink and blue) and the product-bound state (green) opening the active site to the membrane. **b** Time-series representations of SMD simulations initiated from the product-bound state. Ribbon structures are colored as in Fig. 1. Over the course of 200 ns, UndP-Glc exits the active site via W207 rotation and conformational changes in the β7-JM2 loop. On bottom, structural superposition of the initial (t = 0 ns, gray) and final (t = 200 ns, pink and light blue) conformations highlights the lateral displacement of UndP-Glc and the rotational shift of W207, which together facilitate product egress. The approximate membrane position is indicated by a dotted line. **c** Distance plots from SMD simulations tracking key residue interactions with the UndP-Glc headgroup. Each chain in the product-bound model was simulated independently and is represented by these colors: blue, purple, green and red. Initially, R125 coordinates UndP-Glc, but this interaction weakens as the product exits. The K180–UndP interaction is rapidly lost, while W207 initially remains close (0–100 ns) but moves away upon its rotational shift. **d** The apparent binding affinities of GtrB for the indicated compounds were determined by displacing UDP-[^{14}C]-Glc bound to 1.5 μM GtrB. Displacement of 0.25 μM UDP-[^{14}C]-Glc with increasing concentrations of non-labeled compounds yielded the $EC_{50}^{compound}$ (reflecting the concentration of compound at which 50% of the bound UDP-[^{14}C]-Glc was displaced). Data (mean ± s.e.m.; $n = 9$ for all compounds, except for caged-UDP-Glc where $n = 3$) were subjected to one-site fitting algorithms in Prism 10 (GraphPad), and the calculated $EC_{50}^{compound}$ are shown as non-log values (see Supplementary Table 3 for the mean and s.e.m. of the fitting in log scale). **e** Incorporation of 0.25 μM UDP-[^{14}C]-Glc was measured in proteoliposomes containing indicated GtrB variants for 20 min. Data are mean ± s.e.m. ($n = 4$).

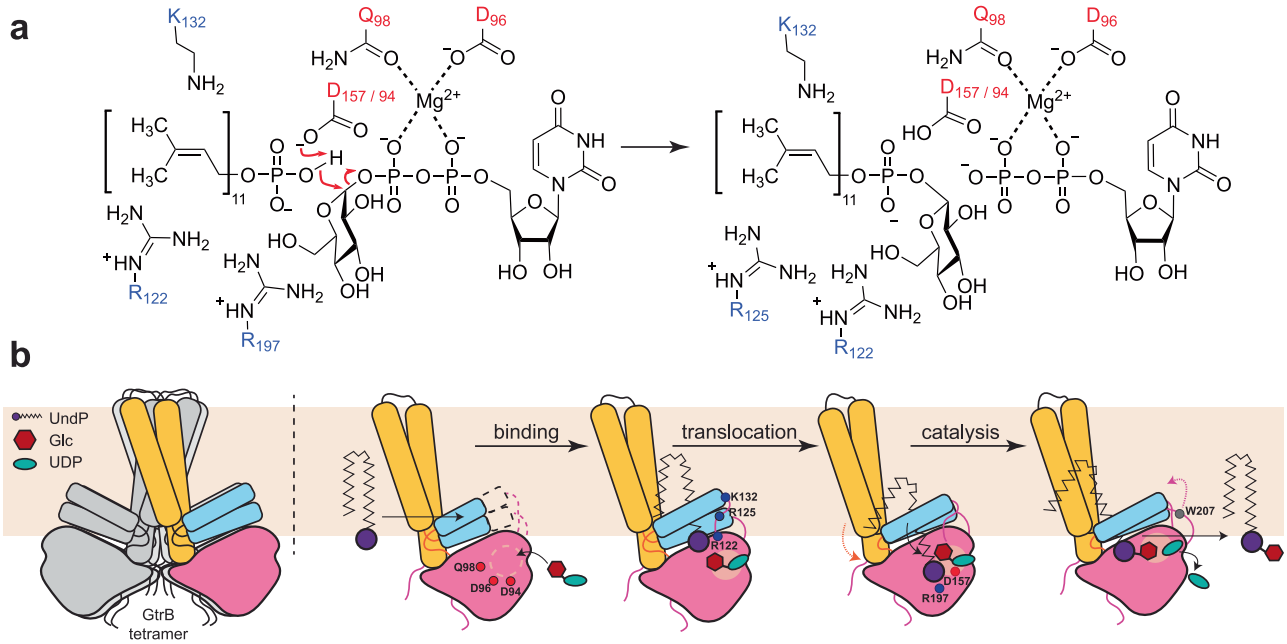

Fig. 5 | Mechanism of catalysis for GtrB. **a** Schematic showing residues within the active site of GtrB around UndP and UDP-Glc. Mg^{2+} is coordinated by the diphosphate of UDP, D96 of the DxD motif, and Q98. UndP is coordinated by K132, R125, R122, and R197. The catalytic base, either D157 or D94, performs the nucleophilic attack on the terminal hydroxyl of UndP, which permits it to attack the C1 of Glc, transferring it onto UndP. **b** Schematic representation of the glycosylation of UndP with UDP-Glc by GtrB, viewed from the side of the membrane. GtrB is shown as a single protomer for simplicity and colored by TM domain (orange), GT domain (pink), and JM helices (light blue). The reaction cycle begins with binding of UndP (purple) and UDP-Glc (teal and maroon) to GtrB causing the ordering of the JM helices by PP binding and UDP being coordinated in the pocket of Q98 and the DxD motif. Then, translocation of UndP by R125, R122, and K132 occurs, lowering JM1 in the process, and bringing the UndP headgroup in proximity to C1 of UDP-Glc. Catalysis occurs shortly after, once the UndP phosphate is coordinated by R197 and the displacement reaction is stimulated by D157 or D94. After transfer of Glc onto UndP, W207 flips outwards opening the β7-JM2 loop and allowing exit of UndP-Glc towards the membrane and recycling of UDP in the cytoplasm.

attributed as the catalytic acid, is D157, which deprotonates UndP for nucleophilic attack on the Glc C1 residue in an S_N2-like displacement reaction (Fig. 5a).

However, unambiguously assigning the catalytic residue is difficult as several amino acids in particular D99 and D94, are at similar distances to the UndP headgroup as D157 in the pre-catalysis state (~ 9 – 10 Å). Our results show low incorporation of [^{14}C]-Glc for the D157N mutant (Fig. 4e), and we were unable to stably incorporate D99 and D94 mutants into proteoliposomes (Supplementary Fig. 12a). While D94 belongs to the universally conserved DxD motif, D157 and D99 are less conserved (Supplementary Fig. 12c). Across homologs of GtrB there is little consensus towards a catalytic residue, but the recent structure of ArnC[23] suggested that the first residue in the DxD motif, corresponding to D94 (D100 in ArnC), acts as the catalytic base. Therefore, whether D157 or D94 is the catalytic residue remains unclear, and this may be enzyme specific.

Discussion

We developed a cryo-TREM approach to visualize the catalytic events during the transfer of Glc onto the lipid carrier UndP by the bacterial membrane glycosyltransferase, GtrB. Exploiting the photolabile properties of a caged substrate allowed us to effectively prevent reaction initiation until milliseconds before vitrification. We determined high-resolution structures of GtrB in a substrate-bound and pre-catalysis state, as well as a product-bound state with UDP and UndP-Glc. The structures reveal how UndP is coordinated within the active site by a set of arginine and lysine residues via its phosphate headgroup. These amino acids subsequently act together to facilitate the movement of UndP towards the Glc moiety for transfer through a reaction involving a catalytic base. The resulting product is then moved back to the hydrophilic binding pocket where it is shuttled out of the active site by a conformational change in a key tryptophan on the solvent-facing loop.

We combined structural variability analysis, MD simulations, and kinetic assays to validate our proposed reaction mechanism and order of events. The assignment of the catalytic residue however remains ambiguous. Despite D157 being previously attributed, our findings suggest that D94 or D99 could also play this role. Consistent with what has recently been proposed for ArnC[23], we consider D94 to be the most likely contender. While the DxD motif typically coordinates the metal ion, D96 along with Q98 appears to take over this role in both the pre-catalysis and product-bound states and in other related membrane-bound GT-A enzymes[18,21,23,35], suggesting D94 could be liberated from metal coordination to act as the catalytic base.

The structural and mechanistic insights into GtrB described here have implications beyond bacterial GTs. Our results reveal some degree of promiscuity in ligand recognition, which could be a mechanism by which these enzymes operate across different species. Furthermore, the structure of GtrB in its substrate- and product-bound states has similarities to the Dolichol Phosphate Mannose Synthase (DPMS) complex found in eukaryotic species[20,21]. DPMS synthesizes the mannose carrier, DolP-mannose, in a reaction functionally identical to the one catalyzed by GtrB[13,24]. However, DPMS operates as a multicomponent system consisting of the soluble GT DPM1 and the transmembrane proteins DPM2 and DPM3[36]. Notably, genetic defects in DPM1 cause Type 1e Congenital Disorders of Glycosylation (CDG1e), resulting in severe developmental delays, seizures, and in some cases, muscular dystrophy in affected children[17,37,38]. Previously, GtrB was shown to readily glycosylate DolP[20]. Comparing the structure and mechanism of GtrB to an archaeal DPMS[21], shows similarities in polyprenyl coordination through JM helices and a flexible solvent-facing JM-loop. However, previous models suggested DolP remains relatively stationary within the DPMS active site, while our data suggest considerable lipidic substrate reorganization during catalysis, highlighting the dynamic nature of these enzymes.

Our time-resolved approach presents both opportunities and challenges for exploring other key intermediate states underlying diverse enzymatic catalytic mechanisms, provided a caged substrate can be synthesized. Accessibility of such intermediate states has been traditionally achieved by using commercial drugs or mutagenesis to bias certain states, at the expense of the physiological context we strive to capture. Similarly, studies capturing large conformational changes[10,11] and dynamics[39] have been achieved with cryo-EM, but enzymes with faster kinetics or proteins not amendable to mutation[40–43] require a different approach. Here, we were dependent on the timescale of the reaction, and we estimated the turnover rate of GtrB to be ~ 200 ms. Thus, we were just within the observable range using our approach and potentially this explains why the substrate-bound state is the predominant conformation in our dataset. Extending time to freezing could allow exploring other conformations after product formation. We anticipate that future work using this method will further demonstrate the potential of capturing enzymatic dynamics for answering mechanistic questions, offering the opportunity to understand how enzymes accommodate substrates to perform catalysis.

Method

Cloning and expression

GtrB from cyanobacterium *Synechocystis* sp. PCC 6803 (accession #Q55487) was cloned into plasmid expression vector pMCSG7 as previously described[20]. Briefly, the open reading frame of GtrB was amplified and cloned into pMCSG7 by ligation-independent cloning, which contains a 6xHis-tag and tobacco etch virus (TEV) protease cleavage site at the N-terminus. All point mutations were prepared by site-directed mutagenesis using primers designed with QuikChange Primer Design Tool (Agilent). All plasmid constructs (Supplementary Table 1). were verified by DNA sequencing and whole plasmid sequencing (sequence alignments were performed using Unipro UGENE[44]).

Protein expression and purification

The GtrB pMCSG7 plasmids were transformed into *E. coli* strain BL21 (DE3) pLysS for overexpression. Detergent-solubilized protein was purified as previously described[20]. Briefly, 800 mL of 2xYT media with 100 µg/mL of ampicillin and 50 µg/mL of chloramphenicol was inoculated 1/100 with overnight culture. Cells were grown at 37 °C until OD_{600} reached 0.8, after which the temperature was reduced to 22 °C and allowed to shake at 200 revolutions per minute (rpm) for 15 min. After which, 0.2 mM isopropyl β-D-thiogalactopyranoside (IPTG) was added, and growth proceeded overnight with shaking (240 rpm). Cells were harvested at 5300 x *g* for 20 min, washed with 40 mL of phosphate-buffered saline (PBS), and frozen at −80 °C for future use. For structural studies, a single pellet (corresponding to 800 mL of culture) was resuspended into 40 mL of lysis buffer containing 20 mM 2-[4-(2-hydroxyethyl)piperazin-1-yl]ethanesulfonic acid (HEPES) pH 7.5, 500 mM NaCl, 10 µg ml^{-1} DNase I, 8 µg ml^{-1} RNase A, 1 mM tris(2-carboxyethyl)phosphine hydrochloride (TCEP), 1 mM phenylmethanesulfonyl fluoride (PMSF), and Complete Mini EDTA-free protease inhibitor cocktail (Roche) used according to the manufacturer's instructions, before being sonicated for 20 min. 1% (w/v) *n*-dodecyl-β-d-maltopyranoside (DDM, Anatrace) was added to the solution to solubilize and rotated at 4 °C for 2 h. Solubilized cells were ultracentrifuged (Beckman Coulter) at 90,500 x *g* for 30 min at 4 °C, the supernatant was then added to a 1 mL solution of Ni-NTA slurry (500 µL total resin, Qiagen) and rotated overnight. Elutate from metal-affinity chromatography was further purified by size-exclusion chromatography using a 24 mL Superdex 200 Increase 10/300 GL column (Cytiva). Peak fractions were extracted and frozen at −80 °C for future use or directly used for nanodisc incorporation.

Preparation of nanodiscs

1-Palmitoyl-2-oleoyl-*sn*-glycero-3-phosphoglycerol (POPG) lipids (Avanti) were stored in a stock of 20 mM HEPES pH 7.5, 100 mM NaCl, and 30 mM Sodium Cholate at 10 mM, dried with Argon gas, and frozen at −80 °C. Commercial undecaprenyl phosphate (Larodan) was resuspended in chloroform at 11.8 mM and dried with argon before adding 10% w/w to POPG and sonicated to ensure proper incorporation. Eluted GtrB was stored in 20 mM HEPES pH 7.5, 150 mM NaCl, 0.05% DDM, 300 mM imidazole, and 1 mM $MgCl_2$. GtrB was incorporated into lipid nanodiscs with a 1:280:5 molar ratio of protein: POPG mixture (POPG and UndP): 1E3D1 (MSPE3D1) in reconstitution buffer (20 mM HEPES pH 7.5, 150 mM NaCl, 1 mM $MgCl_2$, and 1 mM TCEP). This mixture was incubated at 4 °C for 2 h with gentle agitation. Reconstitution was initiated by removing detergent with the addition of Bio-beads (Bio-Rad) at 4 °C overnight with constant rotation. The nanodisc reconstitution mixture was bound again to Ni^{2+}-NTA resin at 4 °C for 4 h to remove empty nanodiscs. The resin was washed with 10 column volumes of wash buffer (20 mM HEPES pH 7.5, 150 mM NaCl, 20 mM imidazole, and 1 mM $MgCl_2$) followed by 4 column volumes of elution buffer (20 mM HEPES pH 7.5, 150 mM NaCl, 300 mM imidazole, and 1 mM $MgCl_2$). The protein was further purified by a Superdex 200 Increase 10/300 GL size-exclusion column in gel filtration buffer (20 mM HEPES 7.5 pH, 150 mM NaCl, 1 mM MgCl2, and 1 mM TCEP). Protein typically eluted as a sharp peak at ~10.5 mL with a neighboring aggregate peak at 8.5 mL, observed by monitoring the absorbance at 280 nm (Supplementary Fig. 1d). Peak fractions were pooled and frozen at −80 °C.

Synthesis of caged-UDP-Glc

All reagents were purchased from commercial sources and used without further purification unless otherwise noted. Solvents used in reactions were purified by passage through alumina and copper

columns under argon. Unless otherwise noted, reactions were carried out at room temperature, under argon and were monitored by TLC on silica gel G-25 F254 (0.25 mm). TLC spots were detected under UV light and charring after staining with p-anisaldehyde in ethanol, acetic acid, and H_2SO_4. Column chromatography was performed on silica gel 60 (40–60 μM) unless otherwise noted. ^{1}H NMR spectra were recorded at 500 MHz and were referenced to the solvent residual proton signal of $CDCl_3$ (7.26 ppm) or D_2O (4.79 ppm). $^{13}C\{^1H\}$ NMR spectra were recorded at 125 MHz and were referenced to $CDCl_3$ (77.06 ppm) or external acetone (31.07 ppm, D_2O). Peak assignments were made based on 2D NMR analysis (^1H–^1H COSY HSQC). High resolution ESI mass spectra were recorded on an Agilent Technologies 6220 spectrometer or a JMS-T100LP AccuTOF LC-plus 4 G TOF mass spectrometer (JEOL, Tokyo, Japan) using samples in CH_3OH and added NaCl. Spectra were obtained by voltage scan over a narrow range at a resolution of approximately 10,000 (Spectra can be found in the Source Data).

1,2,4,6-Tetra-*O*-acetyl-3-*O*-(2′-nitrobenzyl)-β-D-glucopyranose (**S2**): To a solution of diacetone Glc (**S1**, 4.0 g, 15.37 mmol) and tetrabutylammonium bromide (991 mg, 3.07 mmol) in CH_2Cl_2 (20 mL) was added KOH (10 mL, 33% aqueous solution). The resulting mixture was stirred for 10 min and then 2-nitrobenzyl bromide (6.64 g, 30.74 mmol) was added. The solution was stirred for 2 h and then was extracted with CH_2Cl_2 twice. The combined organic phase was dried over Mg_2SO_4, filtered and concentrated. The resulting residue was purified by chromatography (4:1 to 3:1, Hexanes–EtOAc) to afford the product (6.2 g, 93%) as an orange gel. The compound obtained was dissolved in 4:1 AcOH:H2O (40.0 mL), heated at 80 °C for 8 h before the reaction mixture was cooled to room temperature and concentrated. The residue was suspended in Ac_2O (20 mL) and pyridine (15 mL) in presence of catalytic amount of DMAP (202 mg, 1.57 mmol) and the solution was stirred for 10 h. The reaction mixture was concentrated, diluted with EtOAc (60 mL) and then sequentially washed with 1 N HCl, saturated aqueous $NaHCO_3$, and brine. The organic layer was concentrated and the resulting residue was purified by chromatography (2:1, toluene–EtOAc) to yield S2 (4.62 g, 9.52 mmol, 62% over three steps, 2:1 β:α) as an orange gel (Rf 0.29, 2:1, toluene–EtOAc).

Diallyl (2,4,6-tri-*O*-acetyl-3-*O*-(2′-nitrobenzyl)-β-D-glucopyranosyl) phosphate (**S3**): Imidazole (700 mg, 10.31 mmol) was added to compound **S2** (4.15 g, 8.59 mmol) in CH_3OH (45.0 mL), and the solution was heated at 40 °C for 24 h. The reaction mixture was cooled to room temperature, concentrated and then diluted with EtOAc before being washed with brine. The organic layer was dried over Mg_2SO_4, filtered, concentrated and the residue purified by chromatography (1:1, Hexane–EtOAc) to obtain the corresponding hemiacetal intermediate (3.26 g, 7.41 mmol) as white solid. Diallyl *n*-diisopropylphosphoramidite (1.18 ml, 4.6 mmol) and tetrazole (3% in acetonitrile) (26 mL, 13.2 mmol) were added to hemiacetal intermediate (1 g, 2.2 mmol) in anhydrous CH_2Cl_2 (30 mL) under argon and the mixture was stirred for 2 h. After completion of the reaction, the solution was cooled to −40 °C and *t*-butyl hydroperoxide (30% aq., 790 μL, 8.8 mmol) was added. After 1.5 h, the mixture was concentrated and the residue was purified by chromatography (1:1, Hexane–EtOAc) to give **S3** (1.21 g, 2.01 mmol, 91%) as white foam (R_f 0.24, 1:1, Hexane–EtOAc).

3-*O*-(2′-nitrobenzyl)-uridine-5′-diphosphate (**caged-UDP-Glc**): To a solution of **S3** (130 mg, 0.216 mmol) in CH_2Cl_2–CH_3OH (1:1) was added $PdCl_2$ (19 mg, 0.108 mmol). The reaction mixture was stirred for 8 h, neutralized by the addition of Et_3N (100 μL), filtered through Celite, concentrated, dried and taken to next step without further purification. This crude residue was dissolved in pyridine (3 mL), and then UMP-morpholidate (222 mg, 0.324 mmol) and 1*H*-tetrazole (45 mg, 0.65 mmol) were added. The reaction mixture was stirred for 3 days, concentrated and the resulting residue was purified by chromatography (5:2:1, EtOAc–CH_3OH–H_2O). The compound obtained was suspended in CH_3OH (10 mL) and cooled to 0 °C; to this solution 1 M LiOH (1 mL) was added. The reaction mixture was warmed to room temperature and then stirred for 5 h. Excess base present in the reaction mixture was quenched by the addition of IR-120 resin and the solution was filtered and concentrated. The resulting residue was by purified by C_{18} column chromatography (H_2O as eluent) to give **caged-UDP-Glc** (38 mg, 0.055 mmol, 26% over three steps) as a white foam (R_f 0.15, 4:1.5:0.5:0.5 EtOAc–CH_3OH–H_2O–AcO_2H).

Photorelease characterization

Reverse-phase high-performance liquid chromatography (Agilent 1100, C18 column, Eluent A – 95% water, 5% acetonitrile and 0.1% TFA, Eluent B- 95% acetonitrile, 5% water and 0.1% TFA, absorbance at 260 nm) was used to quantify the photorelease of caged-UDP-Glc from the starting material. To generate the standard curve, inosine (100 μM, Sigma-Aldrich) was used as the internal standard due to its stability under UV exposure. Supplementary Fig. 3b shows the plot of the ratio of integrated areas corresponding to the signals from caged-UDP-Glc (no UV) and inosine, versus their concentration ratios. The linear relation between the peak-area ratio and the concentration ratio was used to calculate photoreleased UDP-Glc upon UV exposure. For photorelease quantification, a 75 μL sample containing the caged-UDP-Glc and inosine was deposited in a well of a 96-wellplate. The UV delivery optics were aligned with the center of that well, and the distance between the liquid surface and the collimating lens was adjusted to 15 mm, which is approximately the corresponding value in the vitrification instrument. After an exposure of 17 ms, the sample was collected for HPLC analysis. Supplementary Fig. 3c shows the photoreleased UDP-Glc for two concentrations of the starting caged material. The details of the calculation and the theoretical background of the relation between exposure in the wellplate and in the grid are found in the Supplementary Information. Additionally, to validate the photoproduct signature as well as the stability of the caged material, direct injection ESI mass-spectrometry analysis was performed with samples exposed to room temperature for 24 h and no UV, to 5 s UV, and to no UV fresh. The intensity signals corresponding to the photoproduct (mass 565) and the caged material (mass 700) are shown in Supplementary Fig. 3d.

Cryo-TREM sample preparation

Caged-UDP-Glc (final concentration 2.5 mM) was added to the GtrB solution (1.22 mg/mL; 20 mM HEPES pH 7.5, 150 mM NaCl, 1 mM $MgCl_2$, 1 mM TCEP) immediately before vitrification. Photosensitive material was protected from laboratory light by wrapping the tubes with aluminum foil. A Vitrobot Mark IV (ThermoFisher) was used for freezing the sample EM grids. For the UV (365 nm) activated photorelease of caged-UDP-Glc, the light-guide and collimation optics were installed on the left side of the Vitrobot chamber, as previously described[28]. A 3.5 μL sample was deposited on the glow-discharged copper R1.2/1.3 300-mesh holey carbon grid (Quantifoil) inside the chamber equilibrated to 4 °C and 100% humidity, and immediately blotted for 3.5 s, 4 s and 4.5 s with a blotting force set to 3. To minimize unwanted photoreaction, the chamber light was kept off and the UV was turned on manually when the blotting process had finished, and the blotting arms had retracted back to the rest position. Thus, the grid along with the sample travels through the collimated UV beam for approximately 17 ms before being frozen into liquid ethane cooled by liquid nitrogen. The travel time of grids between the end of UV exposure and the contact with ethane is approximately 55 ms.

Cryo-EM data collection and processing of apo-GtrB

Micrographs were collected with a Technai T30 Polara (FEI), at the Columbia University Cryo-Electron Microscopy Center, equipped with an energy filter and a K3 direct electron detection filter camera (Gatan K3-BioQuantum) with a 0.95 Å nominal pixel size. An energy filter slit

width of 20 eV was used during the collection and was aligned automatically every hour using Leginon[45]. Data collection was performed using a dose of ~70.91 $e^-/Å^2$ across 40 frames (100 ms per frame) at a dose rate of approximately 16 e^-/pix/s, using a set defocus range of −2.5 µm to −1 µm. A 100 µm objective aperture was used. 3757 micrographs were recorded over a one-day collection (Supplementary Table 2).

Movie frames were imported and aligned using Patch Motion Correction implemented in cryoSPARC v.4.6.2. Contrast transfer function (CTF) estimation was performed using Patch CTF. Initial template picking was used, resulting in 946,644 particles, which were then extracted with a 300-pixel box size binned 3 times (Supplementary Fig. 1f). The particles were classified using 2D classification using a batch size per class of 200 with 40 online-EM iterations and one full iteration. 2D classes with well-defined high-resolution features were selected, resulting in a particle stack of 308,978 particles. The particles were then re-extracted using a 360-pixel box size without binning. One round of ab initio reconstruction was performed using three classes, with a maximum resolution set at 7 Å and an initial resolution at 9 Å. This resulted in one class that appeared to be an octamerized GtrB and two classes that were likely junk. We then went back to the binned particle stack of 308,978 particles and ran heterogeneous refinement using the one octamer class from the ab initio reconstruction, two decoy classes, and a "Batch size per class" of 1000. This heterogeneous refinement was run three times using the particles from the three ab initio classes from the previous heterogeneous refinement as input for the next heterogeneous refinement. The octamer class (227,610 particles) was re-extracted without binning and used for non-uniform refinement to yield a resolution of 2.83 Å with D4 symmetry imposed. A mask covering the octamer was used to run a Local Refinement with D4 symmetry and reference-based motion correction to a resolution of 2.79 Å with D4 symmetry imposed.

Cryo-TREM data collection and processing

Images were collected with a Titan Krios electron microscope (FEI), at the Columbia University Cryo-Electron Microscopy Center, equipped with an energy filter and a K3 direct electron detection filter camera (Gatan K3-BioQuantum) with a 0.83 Å nominal pixel size. An energy filter slit width of 20 eV was used during the collection and was aligned automatically every hour using Leginon[45]. Data collection was performed using a dose of ~58.5 $e^-/Å^2$ across 50 frames (50 ms per frame) at a dose rate of approximately 16 e^-/pix/s, using a set defocus range of −2.5 µm to −1 µm. A 100 µm objective aperture was used. 9219 micrographs were recorded over a two-day collection (Supplementary Table 2).

Movie frames were imported and aligned using Patch Motion Correction implemented in cryoSPARC v.4.6.2. Contrast transfer function (CTF) estimation was performed using Patch CTF. Initial particle picks and micrographs were used to train the Topaz neural network particle picking[46] implemented in cryoSPARC resulting in 2,693,490 particles which were then extracted with a 360 pixel box size binned 3 times (Supplementary Fig. 4a). The particles were classified using 2D classification using a batch size per class of 200 with 40 online-EM iterations and one full iteration. 2D classes with well-defined secondary features were selected resulting in a particle stack of 1,457,435 particles. The particles were then re-extracted using a 360-pixel box size without binning. One round of ab initio reconstruction was performed using three classes, with a maximum resolution set at 7 Å and an initial resolution at 9 Å. This resulted in one class that appeared to be an octamerized GtrB and two classes that were GtrB tetramers. We then went back to the binned particle stack of 2,693,490 particles and ran heterogeneous refinement using the three classes from the ab initio reconstruction, two decoy classes, and a "Batch size per class" of 1000. This heterogeneous refinement was run three times using the particles from the three ab initio classes from the previous heterogeneous refinement as input for the next heterogeneous refinement. From this, the class that pertained to the tetramer volume was separated (443,237 particles), further classified with 2D classification to yield 33,816 particles, and extracted with a box size of 300 pixels. These particles were used to refine by Local Refinement using C4 symmetry with a mask to 3.19 Å (Supplementary Fig. 4a). The octamer class (748,694 particles) was subjected to a final heterogeneous refinement using the map from the previous heterogeneous refinement and a 10 Å lowpass filtered map as input. The particles were re-extracted without binning and used for non-uniform refinement to yield a resolution of 2.59 Å. To exploit the inherent symmetry of octamerized GtrB, particles were symmetry expanded to D1, and the 3D center coordinates were adjusted to a single tetramer. Particles were reextracted using a box size of 256 pixels to yield 1,016,679 particles. A mask covering the centered tetramer was used to run a Local Refinement with C4 symmetry to a resolution of 2.42 Å. To classify the dynamics within the dataset, particles were fed into 3D variability analysis with a binary mask (soft padding width: 0) used in the previous refinement with a filter resolution of 4 Å and a high pass resolution of 15 Å with 10 components. Component 0 was displayed by intermediates with a filter resolution of 4 Å and the intermediate window set to −1. Particles from component 0 were further classified by 3D classification with a 4 Å filter and 15 Å high-pass resolution with 10 classes. Classes with the best density for UndP (314,552 particles) were refined with Local Refinement with "Use pose/shift Gaussian prior during alignment" set to true, Standard deviation (deg) of prior over rotation set to 6, Standard deviation (A) of prior over shifts set to 2, and symmetry to C4 to yield a resolution of 2.54 Å and the map we refer to as the substrate-bound state. Classes with lower JM helix density to the previous map were further separated by a 5-class 3D classification with filter resolution set to 3 Å and high pass at 15 Å. A single class (46,382 particles) was refined using the same parameters as before with Local Refinement to a resolution of 2.85 Å containing the pre-catalysis and product-bound states.

Structure model building and refinement

An initial model of GtrB was built using the published GtrB X-ray crystal structure[20]. The model was fitted to the map as a rigid body in ChimeraX[47], the model was subsequently adjusted to the current density and further refined using Coot[48] and PHENIX[49–52], iteratively.

Molecular dynamics system preparation

The starting configurations for GtrB bound to UDP-Glc, Mg^{2+} and UndP in their substrate-bound state were taken directly from the cryo-EM structure of the complex. Intermediates and product configurations were observed in one chain of the complex in different structures. For this reason, models containing the same conformation of the substrates in different configurations were created, duplicating the chain of interest four times, obtaining two different models: pre-catalysis state and product-bound state. In this way, each model contains the same configuration in the four chains of the complex. A key difference between the cryo-EM and simulation models is the length of the UndP substrate. While the experimental density only resolved five isoprenyl units, it was crucial to model the full-length, 55-carbon lipid for the MD simulations to accurately represent the complete substrate and its interactions within a continuous lipid bilayer. To achieve this, the unresolved portion of the tail was computationally built onto the experimentally derived headgroup using Maestro. Crucially, during the subsequent extensive equilibration phase, this modeled tail was left completely unrestrained, allowing it to freely relax and equilibrate its conformation within the lipid bilayer. This ensures that the final dynamics are representative of a physically plausible state and not an artifact of the initial modeled placement. The system was then pre-processed for simulation with the Schrodinger's Protein Preparation Wizard[53] tool, and residue protonation states were determined by

PROPKA at pH = 7.0. The system was embedded in a 141 × 141 Å PPPE − PPPC (75:25 molar ratio) bilayer and solvated using the TIP3P water model with the aid of the membrane-builder tool of CHARMM-GUI[54], and neutralized using K+ and Cl- ions, reaching the 0.1 M salt concentration.

The ff19SB[55] and lipid21[56] Amber force fields were used to parametrize the protein and the lipids, respectively. For the substrate molecules, GAFF2 parameters were adopted. Their atomic partial charges were computed using the restrained electrostatic potential (RESP[57]) fitting procedure. The electrostatic potentials (ESPs) were calculated through Gaussian at the HF/6-31 G* level after optimization of the molecules at the same level. The catalytic Mg^{2+} ion was treated as a non-bonded particle using standard Amber parameters, supplemented with weak harmonic distance restraints to the coordinating oxygen atoms to maintain the experimental geometry, a strategy that shown to help preventing artifacts in several metalloenzymes[58]. The choice of TIP3P water model represents a balance between optimal choice for different components of the system. Previous studies have indeed shown the possibility of using TIP3P in combination with ff19sb protein forcefield, while lipid21 and GAFF2 are extensively validated for use with TIP3P. To rigorously ensure that our conclusions were not dependent on the water model, we performed a full set of cross-validation simulations using the recommended OPC water model (3 independent replicates of 1 μs for each system). As shown in Supplementary Figs. 7 and 8, this validation confirmed the congruence between results obtained with both water models. A summary of the simulation system parameters is provided in Supplementary Table 4.

A multistage equilibration protocol was applied to remove unfavorable contacts and provide a reliable starting point for the subsequent simulations. The system was first subjected to 2000 steps of steepest descent energy minimization, with positional restraints (4000 kJ mol^{-1} nm^{-2} on protein backbone, and substrate heavy atoms; 2000 kJ mol^{-1} nm^{-2} on protein sidechains; 1000 kJ mol^{-1} nm^{-2} on lipid heads) and dihedral restraints on lipids (1000 kJ mol^{-1} nm^{-2}); Then the system was heated from 0 to 100 K in 1 ns in NVT, followed by a heating from 100 to 300 K in NPT with the same restraint as the precedent step; Finally, six steps of equilibration steps were performed, using the protocol suggested by CHARMM-GUI, but with increased simulation time. The total duration of the equilibration protocol was indeed increased to 100 ns. During the equilibration stages restraints were progressively lowered.

Unbiased MD simulations

With structures properly equilibrated, unbiased MD simulations was performed for each system in NPT ensemble, using the Nose-Hoover thermostat[59] to set the temperature to 303.15 K and setting the pressure to 1 bar with the Parrinello–Rahman barostat[60]. A time step of 2.0 fs was used, together with the LINCS[61] algorithm, to constrain all bonds involving hydrogens. Each system was simulated for a total of 2.0 μs.

Steered MD (SMD) simulations

Two sets of constant velocity SMD simulations were performed: 1) starting from the substrate-bound state and pulling the UndP towards the deep pre-catalysis state; 2) starting from the product state and pulling the UndP-Glc out of the binding site. For 1), the collective variable chosen for the description of the desired motion was the distance between the UndP headgroup and the Magnesium ion inside the closest catalytic site (d1). For 2), the CV is the distance between the center of mass of the glycosyl phosphate group of UndP-Glc and K180 α-carbon, roughly corresponding to the inner wall of the catalytic site. In both sets of simulations, positional restraints were applied to the Mg^{2+} ions to prevent artificial destabilization of the catalytic site and to cancel out simulation-induced torque. SMD were performed by harmonically restraining the CV and moving the center of the bias (using a force constant of 2500 kJ mol−1 nm−2) at a constant velocity. In 1), distance d1 was decreased from the initial value (average 1.45 + /− 0.05 nm) to 0.52 nm in 200 ns, corresponding to a pulling velocity of ~0.005 nm/ns. In 2), distance d2 was increased from the initial value (0.68 + /− 0.04 nm) to 3.2 nm in 300 ns, corresponding to a pulling velocity of ~0.008 nm/ns. Then the center of the bias was kept in its final position for 50 additional ns. Each SMD simulation was performed independently on each chain of the tetramer, over three replicates, resulting in a total of 12 replicates. The force applied to the harmonic spring was monitored during each replicate, and the work computed by the bias was calculated. The work profiles for all 12 replicates of each process were collected and are reported in Supplementary Fig. 11. The free energy difference (ΔF) was estimated using the Jarzynski equality by calculating the exponential average over all trajectories. In our analysis, we focus on the trajectory with the lowest total work as a practical representative of the most probable transition path, since these low-work realizations are the dominant contributors to the Jarzynski average. From the SMD work, we estimated the magnitude of the first passage time for the two processes through the Eyring–Polanyi equation: $\tau = \frac{h}{kT} e^{\Delta F^{\backslash dagger}}$, with $\Delta F^{\backslash dagger}$ being the estimated free energy barrier of each process. The free energy barrier is computed as half of the work computed during the simulations, assuming that the simulated process is 2 to 5 orders of magnitude faster than the predicted characteristic time[62]. Estimated free energies from faster pulling (1 nm/ns, 0.1 nm/ns) are also reported in Supplementary Fig. 13 for multiple replicas and two different water models. However, none yielded physically accessible energies, justifying the use of the slower pulling velocities. All MD simulations were performed using Gromacs 2023.3, on the Mare Nostrum 5 pre-exascale EuroHPC supercomputer hosted at BSC-CNS and Leonardo hosted at CINECA. SMDs were performed using the MOVINGRESTRAINT function of PLUMED 2.9.0[63].

GtrB-mediated UDP-Glc binding

Binding of UDP-Glc to GtrB incorporated in nanodiscs was assessed with the scintillation proximity assay (SPA) method[34]. Equilibrium binding of 0.25 μM UDP-[^{14}C]-Glc (300 Ci/mmol, American Radiolabeled Chemicals, Inc.) to 1.5 μM GtrB immobilized to 250 μg of Cu^{2+}-coated Yttrium silicate (YSi) SPA beads (Revvity, Inc.) in 100 μL assay buffer containing 20 mM HEPES 7.5 pH, 150 mM NaCl, and 1 mM $MgCl_2$ was performed in the presence or absence of the following non-radioactive compounds at varying concentrations: UDP, UDP-Glc, caged-UDP-Glc, UDP-Gal, Glc, UDP-Glc plus UndP (note that the UndP concentration was kept constant at 50 μM for this assay). The reactions were performed in individual wells of clear-bottom/white-wall 96-well plates in the dark at 23 °C with vigorous shaking on a vibrating platform for 1 h. The counts per minute (cpm) were determined in the SPA mode of a Wallac 1450 MicroBeta plate counter. The non-proximity background signal was determined for each sample in the presence of 800 mM imidazole, which prevents the interaction of the His-tagged GtrB protein with the Cu^{2+}-coated SPA beads, and the non-proximity cpm was subtracted from the cpm determined in the absence of imidazole to obtain the specific binding activity. The activity of GtrB in the absence of non-labelled compounds was set as 100 %, and data were normalized accordingly. Data ($n = 9$ for all compounds, except caged-UDP-Glc where $n = 3$) are shown as mean ± s.e.m., and fits of binding isotherms were obtained using nonlinear regression algorithms in Prism 10 (GraphPad).

Proteoliposomes (PL) preparation

Detergent-purified GtrB was reconstituted into preformed liposomes composed of *E. coli* total lipids (Avanti Polar Lipids, Inc.) at a protein-to-lipid ratio of 1:80 (w/w) following a previously described method[64]. The lumen of the proteoliposomes was composed of 20 mM HEPES 7.5 pH, 150 mM NaCl, and 1 mM $MgCl_2$. The proteoliposomes were

aliquoted, rapidly frozen in liquid nitrogen, and stored at −80 °C to maintain their stability. All experimental setups used liposomes with the same composition but lacking the GtrB protein as a control. The amount of GtrB in proteoliposomes was assayed with the amido black assay[65].

Determining the GtrB-mediated incorporation of UDP-Glc into the lipid bilayer

Before the assay, 200 μM UndP was added to the proteoliposome membrane by sonication. Incorporation of 0.25 μM UDP-[^{14}C]-Glc (300 Ci/mmol, American Radiolabeled Chemicals, Inc.) was performed in proteoliposomes (~ 5 μg per assay) in 250 μL assay buffer composed of 20 mM HEPES 7.5 pH, 150 mM NaCl, and 1 mM $MgCl_2$. After the indicated time periods, the reactions were quenched by the addition of ice-cold 100 mM KP_i, pH 6.6, 100 mM LiCl and filtered through 0.45 μm nitrocellulose filters (Millipore). Dried filters were incubated in scintillation cocktail, and the retained radioactivity on the filters was determined by scintillation counting (Hidex, SL300). Specific radioactivity of UDP-Glc was confirmed by counting known amounts of UDP-[^{14}C]-Glc and was used to transform decays per minute (dpm) into pmol of UDP-Glc. The GtrB-specific activity was determined by subtracting the background signal (dpm) determined in control liposomes (lacking GtrB) from the dpm measured in GtrB-containing proteoliposomes. Non-linear regression analysis of the data was performed by fitting the data to the Michaelis–Menten equation in GraphPad Prism 10 to obtain the Michaelis-Menten constant (K_m) and the maximum velocity of the reaction (V_{max}). The catalytic turnover number (k_{cat}) was determined from the V_{max} by transforming known amounts of GtrB in the assay to pmol.

Reporting summary

Further information on research design is available in the Nature Portfolio Reporting Summary linked to this article.

Data availability

All raw movie frames have been deposited into the Electron Microscopy Public Image Archive (EMPIAR), with accession code EMPIAR-12683. The density maps for the apo, substrate-bound, pre-catalysis/product-bound and tetramer particles have been deposited into the Electron Microscopy Data Bank (EMDB), with accession codes EMD-49932, EMD-49930, EMD-49931, and EMD-49933, respectively. All models have been deposited in the Protein Data Bank (PDB), with accession codes 9NYE, 9NYC, 9NYD, and 9NYF, respectively. An additional model we refer to as the pre-intermediate state is available on the PDB 9NYK) and EMDB-49935 [https://www.ebi.ac.uk/pdbe/entry/emdb/EMD-49935]. All MD simulation data are available publicly on Zenodo [https://doi.org/10.5281/zenodo.17351373]. All raw gels are available in the Supplementary Information. All graph and NMR source data are provided as a Source Data file. Source data are provided with this paper.

References

1. Benkovic, S. J., Hammes, G. G. & Hammes-Schiffer, S. Free-energy landscape of enzyme catalysis. *Biochemistry* **47**, 3317–3321 (2008).
2. Boehr, D. D., McElheny, D., Dyson, H. J. & Wright, P. E. The dynamic energy landscape of dihydrofolate reductase catalysis. *Science* **313**, 1638–1642 (2006).
3. Zhao, B., Guffy, S. L., Williams, B. & Zhang, Q. An excited state underlies gene regulation of a transcriptional riboswitch. *Nat. Chem. Biol.* **13**, 968–974 (2017).
4. Maria-Solano, M. A., Serrano-Hervas, E., Romero-Rivera, A., Iglesias-Fernandez, J. & Osuna, S. Role of conformational dynamics in the evolution of novel enzyme function. *Chem. Commun. Camb.* **54**, 6622–6634 (2018).
5. Amann, S. J., Keihsler, D., Bodrug, T., Brown, N. G. & Haselbach, D. Frozen in time: analyzing molecular dynamics with time-resolved cryo-EM. *Structure* **31**, 4–19 (2023).
6. Sekhar, A. & Kay, L. E. NMR paves the way for atomic level descriptions of sparsely populated, transiently formed biomolecular conformers. *Proc. Natl. Acad. Sci. USA* **110**, 12867–12874 (2013).
7. Stiller, J. B. et al. Structure determination of high-energy states in a dynamic protein ensemble. *Nature* **603**, 528–535 (2022).
8. Bhattacharjee, S. et al. Time resolution in cryo-EM using a PDMS-based microfluidic chip assembly and its application to the study of HflX-mediated ribosome recycling. *Cell* **187**, 782–796.e23 (2024).
9. Torino, S., Dhurandhar, M., Stroobants, A., Claessens, R. & Efremov, R. G. Time-resolved cryo-EM using a combination of droplet microfluidics with on-demand jetting. *Nat. Methods* **20**, 1400–1408 (2023).
10. Papasergi-Scott, M. M. et al. Time-resolved cryo-EM of G-protein activation by a GPCR. *Nature* https://doi.org/10.1038/s41586-024-07153-1 (2024).
11. Bodrug, T. et al. Time-resolved cryo-EM (TR-EM) analysis of substrate polyubiquitination by the RING E3 anaphase-promoting complex/cyclosome (APC/C). *Nat. Struct. Mol. Biol.* **30**, 1663–1674 (2023).
12. Gangwar, S. P. et al. Kainate receptor channel opening and gating mechanism. *Nature* **630**, 762–768 (2024).
13. Burda, P. & Aebi, M. The dolichol pathway of N-linked glycosylation. *Biochim Biophys. Acta* **1426**, 239–257 (1999).
14. Nothaft, H. & Szymanski, C. M. Protein glycosylation in bacteria: sweeter than ever. *Nat. Rev. Microbiol* **8**, 765–778 (2010).
15. Whitfield, C. & Trent, M. S. Biosynthesis and Export of Bacterial Lipopolysaccharides. *Annu. Rev. Biochem.* **83**, 99–128 (2014). *Vol 83*.
16. Raetz, C. R. H., Reynolds, C. M., Trent, M. S. & Bishop, R. E. Lipid a modification systems in gram-negative bacteria. *Annu. Rev. Biochem.* **76**, 295–329 (2007).
17. Grunewald, S., Matthijs, G. & Jaeken, J. Congenital disorders of glycosylation: a review. *Pediatr. Res.* **52**, 618–624 (2002).
18. Zinkle, A. P., Morgan, R. T., Nygaard, R. & Mancia, F. Structural insights into polyisoprenyl-binding glycosyltransferases. *Structure* https://doi.org/10.1016/j.str.2025.01.003 (2025).
19. Lairson, L. L., Henrissat, B., Davies, G. J. & Withers, S. G. Glycosyltransferases: structures, functions, and mechanisms. *Annu Rev. Biochem.* **77**, 521–555 (2008).
20. Ardiccioni, C. et al. Structure of the polyisoprenyl-phosphate glycosyltransferase GtrB and insights into the mechanism of catalysis. *Nat. Commun.* **7**, 10175 (2016).
21. Gandini, R., Reichenbach, T., Tan, T. C. & Divne, C. Structural basis for dolichylphosphate mannose biosynthesis. *Nat. Commun.* **8**, 120 (2017).
22. Patel, D. H. et al. Cryo-EM SPR structures of Salmonella typhimurium ArnC; the key enzyme in lipid-A modification conferring polymyxin resistance. *Protein Sci.* **34**, e70037 (2025).
23. Ashraf, K. U. *et al*. Structural basis of undecaprenyl phosphate glycosylation leading to polymyxin resistance in Gram-negative bacteria. *bioRxiv* https://doi.org/10.1101/2025.01.29.634835 (2025).
24. Maeda, Y., Tomita, S., Watanabe, R., Ohishi, K. & Kinoshita, T. DPM2 regulates biosynthesis of dolichol phosphate-mannose in mammalian cells: correct subcellular localization and stabilization of DPM1, and binding of dolichol phosphate. *EMBO J.* **17**, 4920–4929 (1998).
25. Lerouge, I. & Vanderleyden, J. O-antigen structural variation: mechanisms and possible roles in animal/plant-microbe interactions. *Fems Microbiol. Rev.* **26**, 17–47 (2002).

26. Korres, H., Mavris, M., Morona, R., Manning, P. A. & Verma, N. K. Topological analysis of GtrA and GtrB proteins encoded by the serotype-converting cassette of Shigella flexneri. *Biochem Biophys. Res. Commun.* **328**, 1252–1260 (2005).
27. Rossmann, M. G., Moras, D. & Olsen, K. W. Chemical and biological evolution of nucleotide-binding protein. *Nature* **250**, 194–199 (1974).
28. Bhattacharjee, B., Rahman, M. M., Hibbs, R. E. & Stowell, M. H. B. A simple flash and freeze system for cryogenic time-resolved electron microscopy. *Front. Mol. Biosci.* **10**, 1129225 (2023).
29. Mannerstedt, K. & Hindsgaul, O. Synthesis and photolytic activation of 6″-O-2-nitrobenzyl uridine-5′-diphosphogalactose: a 'caged' UDP-Gal derivative. *Carbohydr. Res.* **343**, 875–881 (2008).
30. Dubochet, J. The physics of rapid cooling and its implications for cryoimmobilization of cells. *Methods Cell Biol.* **79**, 7–21 (2007).
31. Frank, J. Advances in the field of single-particle cryo-electron microscopy over the last decade. *Nat. Protoc.* **12**, 209–212 (2017).
32. Punjani, A., Rubinstein, J. L., Fleet, D. J. & Brubaker, M. A. cryoSPARC: algorithms for rapid unsupervised cryo-EM structure determination. *Nat. Methods* **14**, 290–296 (2017).
33. Punjani, A. & Fleet, D. J. 3D variability analysis: Resolving continuous flexibility and discrete heterogeneity from single particle cryo-EM. *J. Struct. Biol.* **213**, 107702 (2021).
34. Quick, M. & Javitch, J. A. Monitoring the function of membrane transport proteins in detergent-solubilized form. *Proc. Natl. Acad. Sci. USA* **104**, 3603–3608 (2007).
35. Kendrew, J. C. et al. A three-dimensional model of the myoglobin molecule obtained by x-ray analysis. *Nature* **181**, 662–666 (1958).
36. Maeda, Y., Tanaka, S., Hino, J., Kangawa, K. & Kinoshita, T. Human dolichol-phosphate-mannose synthase consists of three subunits, DPM1, DPM2 and DPM3. *EMBO J.* **19**, 2475–2482 (2000).
37. Imbach, T. et al. Deficiency of dolichol-phosphate-mannose synthase-1 causes congenital disorder of glycosylation type Ie. *J. Clin. Invest.* **105**, 233–239 (2000).
38. Kim, S. et al. Dolichol phosphate mannose synthase (DPM1) mutations define congenital disorder of glycosylation Ie (CDG-Ie). *J. Clin. Invest.* **105**, 191–198 (2000).
39. Chen, B. et al. Structural dynamics of ribosome subunit association studied by mixing-spraying time-resolved cryogenic electron microscopy. *Structure* **23**, 1097–1105 (2015).
40. Menetret, J. F., Hofmann, W., Schroder, R. R., Rapp, G. & Goody, R. S. Time-resolved cryo-electron microscopic study of the dissociation of actomyosin induced by photolysis of photolabile nucleotides. *J. Mol. Biol.* **219**, 139–144 (1991).
41. Berriman, J. & Unwin, N. Analysis of transient structures by cryo-microscopy combined with rapid mixing of spray droplets. *Ultramicroscopy* **56**, 241–252 (1994).
42. Feng, X. et al. A Fast and Effective Microfluidic Spraying-Plunging Method for High-Resolution Single-Particle Cryo-EM. *Structure* **25**, 663–670.e3 (2017).
43. Yoder, N. et al. Light-coupled cryo-plunger for time-resolved cryo-EM. *J. Struct. Biol.* **212**, 107624 (2020).
44. Okonechnikov, K., Golosova, O., Fursov, M. & team, U. Unipro UGENE: a unified bioinformatics toolkit. *Bioinformatics* **28**, 1166–1167 (2012).
45. Suloway, C. et al. Automated molecular microscopy: the new Leginon system. *J. Struct. Biol.* **151**, 41–60 (2005).
46. Bepler, T. et al. Positive-unlabeled convolutional neural networks for particle picking in cryo-electron micrographs. *Nat. Methods* **16**, 1153–1160 (2019).
47. Meng, E. C. et al. UCSF ChimeraX: Tools for structure building and analysis. *Protein Sci.* **32**, e4792 (2023).
48. Emsley, P. & Cowtan, K. Coot: model-building tools for molecular graphics. *Acta Crystallogr Biol. Crystallogr* **60**, 2126–2132 (2004).
49. Afonine, P. V. et al. Real-space refinement in for cryo-EM and crystallography. *Acta Crystallogr. Sect. -Struct. Biol.* **74**, 531–544 (2018).
50. Afonine, P. V. et al. New tools for the analysis and validation of cryo-EM maps and atomic models. *Acta Crystallogr. Sect. -Struct. Biol.* **74**, 814–840 (2018).
51. Williams, C. J. et al. MolProbity: More and better reference data for improved all-atom structure validation. *Protein Sci.* **27**, 293–315 (2018).
52. Liebschner, D. et al. Macromolecular structure determination using X-rays, neutrons and electrons: recent developments in. *Acta Crystallogr. Sect. -Struct. Biol.* **75**, 861–877 (2019).
53. Sastry, G. M., Adzhigirey, M., Day, T., Annabhimoju, R. & Sherman, W. Protein and ligand preparation: parameters, protocols, and influence on virtual screening enrichments. *J. Comput. Aided Mol. Des.* **27**, 221–234 (2013).
54. Hsu, P. C. et al. CHARMM-GUI Martini Maker for modeling and simulation of complex bacterial membranes with lipopolysaccharides. *J. Comput. Chem.* **38**, 2354–2363 (2017).
55. Tian, C. et al. ff19SB: Amino-Acid-Specific Protein Backbone Parameters Trained against Quantum Mechanics Energy Surfaces in Solution. *J. Chem. Theory Comput.* **16**, 528–552 (2020).
56. Dickson, C. J., Walker, R. C. & Gould, I. R. Lipid21: Complex Lipid Membrane Simulations with AMBER. *J. Chem. Theory Comput* **18**, 1726–1736 (2022).
57. Bayly, C. I., Cieplak, P., Cornell, W. D. & Kollman, P. A. A Well-Behaved Electrostatic Potential Based Method Using Charge Restraints for Deriving Atomic Charges - the Resp Model. *J. Phys. Chem.* **97**, 10269–10280 (1993).
58. Hu, L. & Ryde, U. Comparison of Methods to Obtain Force-Field Parameters for Metal Sites. *J. Chem. Theory Comput.* **7**, 2452–2463 (2011).
59. Coughtrie, D. J. & Tew, D. P. The Nose-Hoover looped chain thermostat for low temperature thawed Gaussian wave-packet dynamics. *J. Chem. Phys.* **140**, 194106 (2014).
60. Parrinello, M. & Rahman, A. Polymorphic Transitions in Single-Crystals - a New Molecular-Dynamics Method. *J. Appl. Phys.* **52**, 7182–7190 (1981).
61. Hess, B., Bekker, H., Berendsen, H. J. C. & Fraaije, J. G. E. M. LINCS: A linear constraint solver for molecular simulations. *J. Comput. Chem.* **18**, 1463–1472 (1997).
62. Perisic, O. & Lu, H. On the improvement of free-energy calculation from steered molecular dynamics simulations using adaptive stochastic perturbation protocols. *PLoS One* **9**, e101810 (2014).
63. Tribello, G. A., Bonomi, M., Branduardi, D., Camilloni, C. & Bussi, G. PLUMED 2: New feathers for an old bird. *Comput. Phys. Commun.* **185**, 604–613 (2014).
64. Hagenah, L. M. et al. Additional PfCRT mutations driven by selective pressure for improved fitness can result in the loss of piperaquine resistance and altered physiology. *Mbio.* **15**, e01832-23 (2024).
65. Schaffner, W. & Weissmann, C. A rapid, sensitive, and specific method for the determination of protein in dilute solution. *Anal. Biochem* **56**, 502–514 (1973).

Acknowledgements

This work was supported by NIGMS grant R35GM132120 (To F.M.), NICHD grant 1F31HD118755-01 (To R.T.M.), NIGMS grant R01GM160508 (To M.H.B.S.), and the MCDB Neurodegenerative Disease Fund (To M.H.B.S.). We gratefully acknowledge the assistance of members of the laboratory of F.M., including former members Sabrina Giacometti and Yong Zi Tan for help with apo-GtrB purification, and of the Columbia University cryo-EM facility. We acknowledge the EuroHPC JU for providing computational resources under the awarded project EHPC-EXT-2023E01-025. V.I.P. acknowledges support by NIGMS grants K99 GM123228, R00GM123228 and R35GM150831 during the performance

of this project. This work has been partially funded from the European Union's Horizon 2020 research and innovation program (Marie Skłodowska-Curie grant agreement No. 823780). T.L.L. acknowledges intramural support from Academia Sinica (AS-IA-113-L03), which was used to carry out the synthesis of caged-UDP-Glc. We thank the NMR facilities in the Academia Sinica Institute of Biological Chemistry, the Academia Sinica High-Field NMR Center, funded by Academia Sinica Core Facility and Innovative Instrument Project AS-CFII-111-214 and Academia Sinica BioTreC NMR Center funded by Academia Sinica Core Facility and Innovative Instrument Project AS-NBRPCF-111-201 for support of the synthesis of caged UDP-Glc. M.T.A. is the recipient of an Academia Sinica Postdoctoral Fellowship Award. We acknowledge CINECA for the availability of high-performance computing resources as part of the agreement with the University of Milano-Bicocca. G.D.M. acknowledges the National Biodiversity Future Center (NBFC), funded by the Italian National Recovery and Resilience Plan (PNRR), Project Code CN00000033, CUP I33C22001300007, under the European Union's NextGenerationEU program. We dedicate this work to our co-author Daniele Di Marino, who left us prematurely.

Author contributions

V.I.P. and K.U.A. purified protein for the apo cryo-EM sample and performed nanodisc incorporation. V.I.P. prepared grids and collected data for the apo cryo-EM sample. R.T.M. processed and analyzed the cryo-EM data. A.R. optimized expression of the GtrB construct with help from R.T.M. and I.B. A.R. purified protein for time-resolved cryo-TREM sample preparation. Synthesis of caged-UDP-Glc was conducted by M.T.A., B.M., and T.L.L. B.B. and M.H.B.S. designed and tested the second-generation flash and freeze plunge system and the offline quantification system, B.B. determined the experimental and theoretical yields of UDP-Glc following photolysis, determined photoproducts by mass spectrometry and prepared cryoEM grids. R.T.M. collected, processed, and analyzed the cryo-EM data. R.T.M. built the models with help from R.N. Gene editing for *E. coli* functional assays was performed by R.T.M. and E.G. performed protein expression and purification for kinetic assays. E.G. and M.Q. performed all kinetic assays. All MD simulations were performed by S.M., G.D.M., and D.D.M. All authors helped design experiments, and R.T.M., R.N., F.M. wrote the paper with edits and comments from all authors. Oversight for the entire project was provided by R.N. and F.M.

Competing interests

The authors declare no competing interests.

Additional information

Supplementary information The online version contains supplementary material available at https://doi.org/10.1038/s41467-025-66769-7.

Correspondence and requests for materials should be addressed to Michael H. B. Stowell, Rie Nygaard or Filippo Mancia.

Peer review information *Nature Communications* thanks the anonymous reviewers for their contribution to the peer review of this work. A peer review file is available.